JOURNAL OF COMPUTATIONAL PHYSICS 114, 100–112 (1994)

Drift Wave Turbulence in a Plasma with Sheared Flow*

K. L. SIDIKMAN† AND B. A. CARRERAS

Oak Ridge National Laboratory, Oak Ridge, Tennessee 37831-8071

AND

L. GARCIA

Universidad Carlos III, Madrid, Spain

Received June 7, 1993; revised December 1, 1993

A single-equation model of long-wavelength drift waves has been used to study the behavior of turbulent plasma fluctuations in the presence of sheared flow. These waves, which have a real frequency, are calculated using a time-evolution algorithm that includes flow effects. Linear tests show that growth rates and flow-shear damping agree with the predictions of analytical theory, even in the presence of a large real frequency. Criteria for selecting the proper spatial and temporal resolution for nonlinear calculations are described. Convergence tests show that, within these limits, solutions have a weak dependence on variations of these resolution parameters. Tests of energy conservation indicate that calculated solutions remain accurate for large numbers of time steps. © 1994 Academic Press, Inc.

I. INTRODUCTION

The behavior of turbulent fluctuations in the presence of a sheared flow is a subject that has great potential for advancing understanding of magnetic plasma confinement [1]. Experiments with different magnetic configurations naturally develop similar shear layers in the poloidal flow at the edge [2]. In each case, the layer marks the boundary of the region of good confinement and controls local fluctuation levels and transport. The transition from a low confinement regime (L-mode) to a high confinement regime (H-mode) [3] is characterized by an increase in poloidal flow shear [4] and a reduction in fluctuation level [5]. A scaling theory of fluctuation suppression by poloidal flow shear [6] and a linear analysis both predict that turbulence should be strongly stabilized by a sheared poloidal flow.

* Research sponsored by the Office of Fusion Energy, U.S. Department of Energy, under Contract DE-AC05-84OR21400 with Martin Marietta Energy Systems, Inc.

† Supported by an appointment to the U.S. DOE Fusion Energy Postdoctoral Research Program administered at Oak Ridge Institute for Science and Education.

We have studied the effect of a constant flow shear on fluctuations using a single-equation representation of plasma drift waves [7]. These arise naturally from equilibrium density and temperature gradients and have experimentally relevant values of real frequency. Numerical calculations showed the predicted damping of the fluctuations by the flow shear during the linear phase, but the saturation level in the nonlinear regime remained unaffected. Even flow shear large enough to produce complete linear stability had no effect on the saturation level generated nonlinearly. This numerical result confounded expectations from scaling theory and nonlinear analytic theory and forced a reexamination of the latter. We found that spatial structure in the nonlinear couplings between long-wavelength and short-wavelength modes near a low-order rational surface could account for these observations. Further numerical calculations with a single rational surface reinforced this physical picture.

Throughout this investigation, numerical calculations have played a key role in advancing our understanding of the physics. There is already a substantial body of numerical results for drift waves in two [8–10] and three [11] dimensions. In our case, the introduction of a strong flow shear greatly affects the resolution requirements. Time-step restrictions arise owing to large local flows. The radial grid size must be adequate to handle a singularity in the equation. In this paper, we undertake a detailed study of the numerical calculations. The implicit linear algorithm will be shown to give accurate solutions for unstable modes with a real frequency over a wide range of time-step sizes. The predicted damping effect of flow shear will also be reproduced. Resolution requirements for nonlinear calculations will be described, and results from convergence and energy-conservation tests will show that it is possible to address the flow-shear issues and obtain converged and accurate results with reasonable resolution. Thus, this algo-

0021-9991/94 $6.00

rithm proves to be a useful tool for studying fluctuations with nonzero real frequency in the presence of strong flow shear.

The body of the paper is organized as follows. Section II presents the model equation and the solution geometry. The discrete algorithm and its implementation are described in Section III, along with the calculation of numerical errors. Section IV details basic linear tests. In Section V, issues of spatial resolution are addressed, while Section VI is concerned with the size of the time step. Conclusions are presented in Section VII.

II. EQUATIONS AND GEOMETRY

The single model equation to be solved was derived as a paradigm of plasma drift waves at long wavelengths [7]. The plasma ions are taken to be a cold fluid. Their dynamics are governed by a continuity equation for the density, and equations for momentum balance parallel and perpendicular to the magnetic field. A collisional drag is used in the parallel momentum balance equation to provide linear damping of sound waves. The electron physics is primarily determined by the Boltzmann relation between density and potential fluctuations: $\tilde{n}_e/n_{e0} = |e|\,\tilde{\phi}/T_e$, with equilibrium electron density n_{e0} and electron temperature T_e. Electrons trapped in the magnetic ripple along a field line contribute a small phase shift between density and potential that drives wave growth. The shift is derived from a laminar kinetic equation in the dissipative trapped electron regime [12]. Attention is focused on strongly dissipative modes with long wavelengths. Quasineutrality is then used to equate electron and ion density fluctuations. Finally, the added assumption of highly collisional ions permits reduction to a single equation, which is tractable both analytically and numerically.

This equation is solved in slab geometry. The straight slab is a local approximation to a torus, centered on minor radius $r = r_0$ (Fig. 1). With a major radius given by R_0, the local inverse aspect ratio is defined to be $\varepsilon = r_0/R_0 \ll 1$. Within the slab, position is defined with respect to a set of rectangular unit vectors related to the local toroidal directions: $\hat{x}$ to the direction of equilibrium gradients, $\hat{y}$ to the poloidal direction, and $\hat{z}$ to the toroidal direction. The x coordinate, defined by $x = r - r_0$, covers a radial interval of size a: $-(a/2) \leqslant x \leqslant +(a/2)$. At the boundaries, fluctuating quantities are required to go to zero. The y and z coordinates can be related to θ and ζ, the poloidal and toroidal angles:

$$y = r_0\theta, \qquad z = R_0\zeta. \tag{1}$$

Limits on y and z are chosen to correspond to a full cycle of the angular coordinates, and fluctuations are required to be periodic in these directions.

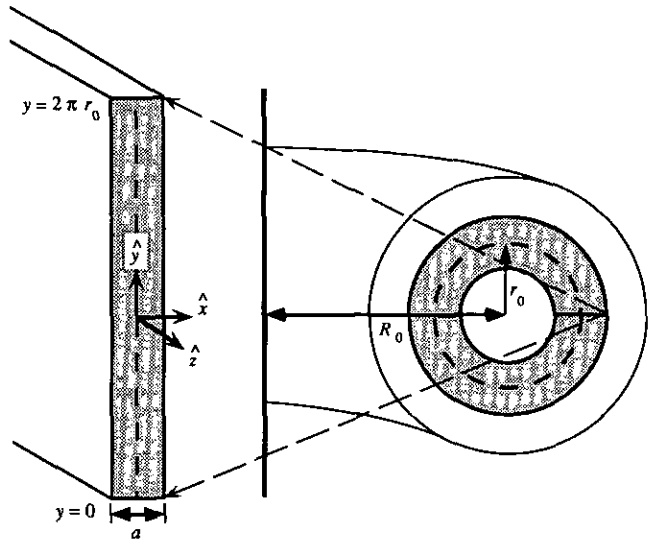

FIG. 1. Slab geometry (left), and its relation to toroidal geometry around minor radius $r = r_0$ (right).

The equilibrium magnetic field is given by $\mathbf{B} = B_0\hat{z} + B_y(x)\,\hat{y}$, with constant B_0 and

$$B_y(x) = B_y(r_0) + B_0\frac{x}{L_s}. \tag{2}$$

The x-dependence of B_y permits the "twist" of a field line to change, thus incorporating magnetic shear into the model. A related quantity, safety factor $q(x) = \varepsilon B_0/B_y(x)$, is used to define the characteristic shear length: $L_s = (q^2/\varepsilon)(dq/dx)^{-1}$. We choose $q_0 = 1.5$ at $r = r_0$, so that the center of the slab is a rational surface (q is a rational number there). Note that the x-variation in q permits calculations with multiple rational surfaces.

Other equilibrium quantities are specified by their magnitudes and scale lengths. These are held constant in the slab. Scale lengths for electron density, n_{e0}, and temperature, T_e, are defined to be $L_n = n_{e0}(dn_{e0}/dx)^{-1}$ and $L_{Te} = T_e(dT_e/dx)^{-1}$, respectively. When an equilibrium velocity is introduced to study flow-shear effects, a profile linear in x is used:

$$V_0(x) = \bar{V}_0\frac{x}{L_V}. \tag{3}$$

These equilibrium profiles are also held fixed in time. This prevents a fluctuation-driven relaxation of the instability drive and ensures that the nonlinear evolution is dominated by turbulent processes.

Now we can write the specific form of the drift-wave equation for the given geometry and equilibrium. The time

evolution of normalized ion density fluctuations $\tilde{n} = \tilde{n}_i/n_{i0}$ is governed by

$$\frac{d}{dt}(\tilde{n} - \rho_s^2 \nabla_\perp^2 \tilde{n}) + V_{*n}\frac{\partial \tilde{n}}{\partial y} + D_k \frac{\partial^2 \tilde{n}}{\partial y^2} - \frac{c_s^2}{\nu_i}\nabla_{||}^2 \tilde{n} - \rho_s c_s \left[\nabla_\perp \left(\frac{D_k}{V_{*n}}\frac{\partial \tilde{n}}{\partial y}\right) \times \hat{z}\right] \cdot \nabla_\perp \tilde{n} = 0. \quad (4)$$

Parallel gradients ($\nabla_{||}$) are defined relative to **B**, and perpendicular gradients ($\nabla_\perp$) are defined relative to $\hat{z}$. The basic time and length scales are the cyclotron frequency $\Omega_i = |e| B_0/m_i$ and gyroradius $\rho_s = c_s/\Omega_i$ for ions of mass m_i, where the sound speed is $c_s = (T_e/m_i)^{1/2}$. Once lengths and times have been normalized to these scales, the rest of the problem can be determined by specifying a few dimensionless parameters. Values for those parameters independent of L_n are listed in Table I. Parameters that vary with L_n are specified in Table II, for the two values of L_n considered.

The role of each term in the above equation can be identified. The convective derivative in the first term gives the time evolution of the fluctuations. It also contains the equilibrium poloidal velocity

$$\frac{d}{dt} \equiv \frac{\partial}{\partial t} + V_0(x)\frac{\partial}{\partial y}. \quad (5)$$

The second term is the diamagnetic drift, with electron drift velocity $V_{*n} = c_s \rho_s / L_n$. This contributes the real part of the frequency. The term after this is the instability drive. The coefficient D_k is related to the nonadiabatic response of the trapped electrons. It is most easily expressed in Fourier space, in terms of poloidal wave number (k_y):

$$D_k = \frac{D_0}{1 + (k_y D_0 / V_{*n})^2}. \quad (6)$$

TABLE I

Values of the Parameters That Characterize the Geometry and Equilibrium in the Numerical Calculations

Parameter	Normalized value
Local inverse aspect ratio	$\varepsilon = 0.1$
Local minor radius	$\frac{r_0}{\rho_s} = 276.7$
Magnetic shear length	$\frac{L_s}{\rho_s} = 5534.0$
Velocity shear length	$\frac{L_V}{\rho_s} = 5.5$
Ion collision frequency	$\frac{\nu_i}{\Omega_i} = 4.16 \times 10^{-6}$

TABLE II

Values of the Parameters That Vary with L_s/L_n, for the Two Cases Considered in the Numerical Calculations

Parameter	Large L_s/L_n case	Small L_s/L_n case
Density scale length	$\frac{L_n}{\rho_s} = 91.3$	$\frac{L_n}{\rho_s} = 276.7$
Drive strength	$\frac{D_0}{c_s \rho_s} = 2.33 \times 10^{-1}$	$\frac{D_0}{c_s \rho_s} = 2.54 \times 10^{-2}$
Velocity magnitude	$\frac{\bar{V}_0}{c_s} = 1.30 \times 10^{-2}$	$\frac{\bar{V}_0}{c_s} = 4.33 \times 10^{-3}$
	$\frac{\bar{V}_0}{c_s} = 2.60 \times 10^{-2}$	
Normalized shearing rate	$\Omega_s(m = 21) = 0.44$	$\Omega_s(m = 40) = 0.29$
(m from fastest-growing mode)	$\Omega_s(m = 21) = 0.88$	

The constant D_0 includes the fraction of trapped electrons ($\sqrt{\varepsilon}$), their effective collision frequency (ν_{eff}), and $\eta_e = L_n/L_{T_e}$:

$$D_0 = 1.5\sqrt{\varepsilon}\,\eta_e (V_{*n}^2/\nu_{\text{eff}}). \quad (7)$$

Next comes the collisional damping of parallel sound waves by ions with collision frequency ν_i. The final term is the convective nonlinearity arising from the nonadiabatic electron response. It is worth noting that the equation contains no viscosity or other form of "artificial" dissipation. Short-wavelength modes are stabilized by the combination of collisional dissipation and decreased drive, given the form of D_k defined in Eq. (6). These stable modes then act as the energy sink.

Numerical solutions of the discrete form of the model equation will develop errors due to finite spatial and temporal resolution. Questions of accuracy can be addressed by considering an independent evolution equation. One such equation governs the evolution of the energy:

$$E = \tfrac{1}{2}\int d^3x (\tilde{n}^2 + \rho_s^2 |\nabla_\perp \tilde{n}|^2). \quad (8)$$

It is obtained from Eq. (4) by multiplying by $\tilde{n}$ and integrating over space:

$$\frac{dE}{dt} = \int d^3x\, D_k \left(\frac{\partial \tilde{n}}{\partial y}\right)^2 - \frac{c_s^2}{\nu_i}\int d^3x\, (\nabla_{||}\tilde{n})^2 + \rho_s^2 \int d^3x \frac{dV_0}{dx}\left(\frac{\partial \tilde{n}}{\partial y}\frac{\partial \tilde{n}}{\partial x}\right). \quad (9)$$

On the right, the first integral is associated with the instability drive; it is an energy source (SO). The second term comes from collisional damping; it is an energy sink (SK). The third integral (VC) comes from the convection of the z-component of vorticity ($-\rho_s^2\nabla_\perp^2\tilde{n}$) by the equilibrium flow. The nonlinear contribution

$$\partial_t E|^{\text{nonlinear}} \equiv \rho_s c_s \int d^3x\, \tilde{n}\left[\nabla_\perp\left(\frac{D_k}{V_{*n}}\frac{\partial\tilde{n}}{\partial y}\right)\times\tilde{z}\right]\cdot\nabla_\perp\tilde{n} \qquad (10)$$

is identically zero. Energy is the only quadratic form conserved by this nonlinearity. Error accumulation in numerical solutions will be checked by monitoring energy conservation, using both Eq. (9) and Eq. (10).

III. NUMERICAL IMPLEMENTATION

Numerical solution of the model equation requires the definition of a discrete computational domain. In the y- and z-directions, we transform to the periodic angular coordinates defined in Eq. (1). Then the density fluctuations can be represented by a discrete Fourier series, with the mode numbers m and n related to the wave numbers $k_y = m/r_0$ and $k_z = n/R_0$:

$$\tilde{n}(x,\theta,\zeta) = \sum_m \sum_{n>0} [\tilde{n}_{m,n}(x)\cos(m\theta+n\zeta) + \tilde{n}_{-m,-n}(x)\sin(m\theta+n\zeta)]. \qquad (11)$$

The differential operators acting on these fluctuations take the form

$$\nabla_\perp^2 = \frac{\partial^2}{\partial x^2} - \frac{m^2}{r_0^2} \quad \text{and} \quad \nabla_{||} = ik_y\left(\frac{n}{m}-\frac{1}{q}\right). \qquad (12)$$

Modes with $m/n = q(r_s)$ can resonate with the magnetic field at rational surface $r = r_s$, since they have $k_{||} = 0$ there. Operations are performed exclusively in (m, n) space, and the results are stored in spectral form. Those pairs of modes that couple to each m, n are identified. As a result, the nonzero contributions to the nonlinear term for a given m, n can be calculated directly from the Fourier components of these mode pairs [13].

The x-dependent Fourier components are represented on a discrete grid. First and second derivatives are calculated using three-point finite difference formulas. These permit unequal spacing between grid points, so the grid can be concentrated in regions with large gradients. A sparse grid has been used only at the edges of the slab, away from any resonant surface in the calculation. Equal spacing is used in all regions with appreciable fluctuations, and the three-point formulas reduce to centered differencing.

The discretized equations are advanced in time using a code called DTEM, a version of the FAR code [14] modified to accommodate sheared slab geometry and the single equation for a single field. Every (m, n) mode is linearly uncoupled from all the others in this geometry. Thus, the discrete form of Eq. (4) can be written symbolically for a given mode as

$$L_{m,n}\frac{\partial X_{m,n}}{\partial t} = R_{m,n}X_{m,n} + N_{m,n}(X). \qquad (13)$$

$X_{m,n}$ is a vector whose elements are the values of $\tilde{n}_{m,n}$ at the radial grid points; $L_{m,n}$ and $R_{m,n}$ are matrix operators with a tridiagonal structure resulting from the three-point radial differencing. The nonlinear term is represented by the vector $N_{m,n}$, whose elements are the convolution values at the radial grid points. Two different algorithms have been used to evolve $X_{m,n}$ by stepping over intervals of size Δt. In both, the advance from step i to step $i+1$ is linearly implicit and nonlinearly explicit. The nonlinearity in the "one-step" scheme is evaluated at the old step i:

$$\left(L_{m,n}-\frac{\Delta t}{2}R_{m,n}\right)X_{m,n}^{i+1} = \left(L_{m,n}+\frac{\Delta t}{2}R_{m,n}\right)X_{m,n}^{i} + \Delta t\, N_{m,n}(X^i). \qquad (14)$$

Solutions are accurate to order Δt. In the "two-step" algorithm, there is first an advance to $i+\frac{1}{2}$. The nonlinear term in the second step is then evaluated at this time, giving solutions that are accurate to order $(\Delta t)^2$:

$$[1]\quad \left(L_{m,n}-\frac{\Delta t}{2}R_{m,n}\right)X_{m,n}^{i+1/2} = L_{m,n}X_{m,n}^{i} + \frac{\Delta t}{2}N_{m,n}(X^i)$$

$$[2]\quad \left(L_{m,n}-\frac{\Delta t}{2}R_{m,n}\right)X_{m,n}^{i+1} = \left(L_{m,n}+\frac{\Delta t}{2}R_{m,n}\right)X_{m,n}^{i} + \Delta t\, N_{m,n}(X^{i+1/2}). \qquad (15)$$

Since the linear part of either scheme is implicit, any linear calculation should be numerically stable for all Δt. The size of the time step is determined by the need to resolve a particular physical time-scale. In general, nonlinear processes impose the greatest restrictions. Section VI will address this issue in detail.

In order to produce a meaningful test of energy conservation, the integrals in Eqs. (9) and (10) must be evaluated in a way that inverts the specific form of differencing used in the model equation. This minimizes the amount of error introduced by the finite resolution of the integration scheme

itself. This point can be illustrated by a calculation of the nonlinear contribution to the energy evolution, defined in Eq. (10). As stated there, the result should be zero. Inverting the time evolution requires multiplying the nonlinearity vector $N_{m,n}$ by the fluctuation vector $X_{m,n}$ at the same time step. For the radial integration, we define a uniform grid with $J+1$ grid points, so that $\Delta x = a/J$ and $x_j = \Delta x(j - J/2)$ for $j = 0, ..., J$. On this grid, the Fourier components can be represented as $f_j = X_{m,n}(x_j)$ and $g_j = X_{-m,-n}(x_j)$ and the convolutions as $F_j = N_{m,n}(x_j)$ and $G_j = N_{-m,-n}(x_j)$. Then, the proper form for the discrete integral at time step s is

$$\partial_t E|_s^{\text{nonlinear}} = (2\pi^2 r_0 R_0) \sum_m \sum_{n>0} \sum_{j=1}^{J} \Delta x\, (f_j F_j + g_j G_j), \tag{16}$$

where $s = i$ for the one-step scheme and $s = i + \frac{1}{2}$ for the two-step scheme. With centered differencing, the terms in the radial sum take the form

$$f_j F_j \approx \left(\frac{b_{j+1} - b_{j-1}}{2\Delta x} c_j + b_j \frac{c_{j+1} - c_{j-1}}{2\Delta x}\right) f_j + b_j c_j \frac{f_{j+1} - f_{j-1}}{2\Delta x}, \tag{17}$$

where b_j and c_j are Fourier components for modes which beat to m, n. The third term in $(f_j F_j)$ does not contain f_j. However, there are contributions with f_j from the corresponding terms in $(f_{j-1} F_{j-1})$ and $(f_{j+1} F_{j+1})$. For the discrete integral of Eq. (16) to sum to zero, as required by Eq. (10), all contributions proportional to f_j must be able to add directly over the interior grid points. Thus, an unweighted sum over radial grid points properly inverts the centered differencing used in the discrete equation.

Once the integral has been defined in this way, Eq. (16) can be used to study the effects of finite spatial resolution on energy conservation. Even though the discrete integral properly inverts the spatial differencing, any real calculation will never vanish exactly. Choosing maximum and minimum m and n introduces an error through truncation of the Fourier sums. When contributions from radial grid points j, $j-1$, and $j+1$ are summed, it becomes clear that complete inversion of the bracket in Eq. (17) requires $c_j \equiv (c_{j+1} + c_{j-1})/2$ and $b_j \equiv (b_{j+1} + b_{j-1})/2$. Failure to satisfy these relations produces an error that depends on Δx. These instantaneous errors can be accumulated over the time evolution to provide a measure of the violation of energy conservation caused by spatial discretization. The "spatial discretization error" at time $t = I\,\Delta t$ is defined from Eq. (16) as

$$(\delta E)_{\text{SD}} = \frac{1}{E(I\,\Delta t)} \sum_{i=0}^{I-1} \Delta t\, (\partial_t E|_s^{\text{nonlinear}}), \tag{18}$$

where $E(t)$ will be defined in Eqs. (19)–(20). Since the components in Eq. (17) are all evaluated at the same time step, the spatial operations produce no term of order Δt in the integrand. Integration then ensures that temporal discretization (nonzero Δt) makes a higher-order contribution. The spatial discretization error depends most sensitively on the number of components in the Fourier representation and the size of Δx. Thus, it can be used to monitor the accuracy of numerical solutions as spatial resolution is varied.

A second test of energy conservation comes from evaluating Eq. (9) with the numerical solutions. At time step i, the radial integrals giving the contribution of each component to the energy (E), source (SO), sink (SK), and vorticity convection (VC) are properly defined by

$$\begin{aligned} E_{m,n} &= \sum_{j=1}^{J} \Delta x \left[\rho_s^2 (f_j')^2 + \left(1 + \frac{m^2 \rho_s^2}{r_0^2}\right)(f_j)^2\right] \\ SO_{m,n} &= D_k \sum_{j=1}^{J} \Delta x \left[\left(\frac{m}{r_0}\right) f_j\right]^2 \\ SK_{m,n} &= \frac{c_s^2}{\nu_i} \sum_{j=1}^{J} \Delta x \left[\left(\frac{\varepsilon}{r_0}\right)\left(n - \frac{m}{q(x_j)}\right) f_j\right]^2 \\ VC_{m,n} &= \rho_s^2 \left(\frac{m}{r_0}\right) \sum_{j=2}^{J-1} \Delta x \left(\frac{f_j + f_{j-1}}{2}\right)(V_0')(g_j'), \end{aligned} \tag{19}$$

with radial derivative $f_j' = (f_j - f_{j-1})/\Delta x$. Integrals over the other two directions are transformed into Fourier sums. The energy becomes

$$E(i\,\Delta t) = (\pi^2 r_0 R_0) \sum_m \sum_{n>0} (E_{m,n} + E_{-m,-n}). \tag{20}$$

The other terms are similarly defined, but with $2\pi^2 r_0 R_0$ multiplying the Fourier sums. Finite spatial and temporal resolution in the numerical solutions produces an imbalance between dE/dt and the energy transfer $TR \equiv SO - SK + VC$. We integrate this imbalance to obtain the "energy conservation error" at $t = I\,\Delta t$:

$$(\delta E)_{\text{EC}} = \left(\frac{E(I\,\Delta t) - E(0)}{E(I\,\Delta t)}\right) - \frac{\Delta t}{2}\left(\frac{TR(I\,\Delta t) + TR(0)}{E(I\,\Delta t)}\right) - \frac{1}{E(I\,\Delta t)} \sum_{i=1}^{I-1} \Delta t\, TR(i\,\Delta t). \tag{21}$$

This measure of the violation of energy conservation comes from the time evolution of a quadratic quantity. Since the terms are evaluated with fluctuations from an independent evolution equation, this error should be more sensitive to the effects of nonzero Δt than the spatial discretization error. Thus, it can detect inaccuracies introduced by both spatial and temporal discreteness. In future sections, the

energy conservation error will be used to monitor error accumulation as a function of time step.

The DTEM code that implements this numerical scheme has features that allow for a natural extension of the problem. For example, the mode couplings produced by the θ-dependence of a toroidal magnetic field can be incorporated in this slab geometry. The block structure of the $L_{m,n}$ and $R_{m,n}$ matrices has been arranged so that all values of m for a particular n are grouped together. Then, when $B_z = B_0(1 - \epsilon \cos\theta)$ is introduced to represent the toroidal field, the coupling of poloidal harmonics m for a particular toroidal mode n is readily accommodated. In addition, it is easy to increase the number of equations and variables used. Elements in the $L_{m,n}$ and $R_{m,n}$ matrices are assigned by subroutines called "blocks." These subroutines catalogue matrix locations by equation number, variable number, and number of derivatives. Once the required storage locations have been defined, new equations can be coded exactly as written, by subsequent calls to blocks. All of this permits a large amount of flexibility.

IV. BASIC LINEAR TESTS

As a basic test of the numerical scheme, we compare calculated linear solutions to the predictions of analytic theory. The analytic solutions have been obtained from standard drift wave theory [15], modified to include the effects of a velocity profile. The dispersion relation for the Doppler-shifted frequency $\bar{\omega} \equiv \omega - k_y V_0(r_s)$ at rational surface r_s is

$$\bar{\omega} = \frac{\omega_{*n}}{1 + k_y^2 \rho_s^2}\left[1 + i\frac{k_y^2 D_k}{\omega_{*n}} - i\left(\frac{\xi_k^2 \rho_s^2}{W_k^4}\right) - (2l+1)\left(\frac{i+1}{\sqrt{2}}\right)\sqrt{\frac{\bar{\omega}}{\omega_{*n}}}\frac{\rho_s^2}{W_k^2}\right], \tag{22}$$

where $\omega_{*n} = k_y V_{*n}$ is the drift frequency, l the radial mode number, and

$$W_k^4 = \omega_{*n} \nu_i (\rho_s L_s / k_y c_s)^2 \tag{23}$$

gives the mode width. Flow shear introduces an eigenfunction shift [7]

$$\xi_k \equiv W_k^3 \Omega_s / 2\rho_s^2, \tag{24}$$

related to the normalized shearing-rate

$$\Omega_s = k_y V_0' W_k / \omega_{*n}, \tag{25}$$

which leads to a new damping term in Eq. (22) (third term in bracket).

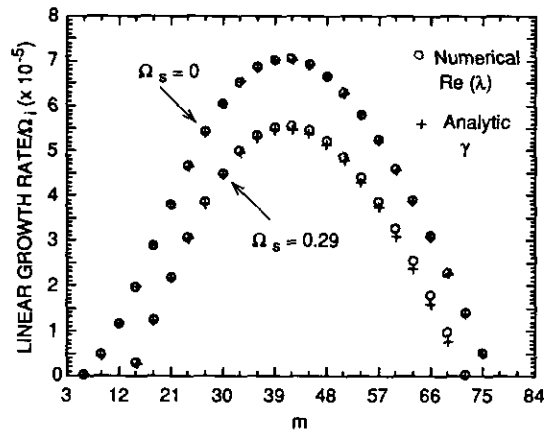

FIG. 2. Analytic growth rate γ and numerical eigenvalue Re(λ) for the linear model, as a function of poloidal mode number m. The agreement is good with flow shear ($\Omega_s = 0.29$) and without ($\Omega_s = 0.00$), for small L_s/L_n parameters.

Results from analytic and numerical calculations are in excellent agreement. The analytic results were obtained from Eq. (22) with $l = 0$. Numerical results came from the linear part of Eq. (14) with a large time step: $\Omega_i \Delta t = 10{,}000$. Small L_s/L_n parameters were used in both cases. For growing modes, the analytic growth rate γ and numerical eigenvalue Re(λ) agree well at all m (Fig. 2). This holds both with and without flow shear, implying that the additional damping calculated for the numerical solutions is the same as that predicted analytically. Good agreement is also evident for the corresponding real frequencies, ω_R and Im(λ) (Fig. 3).

Flow shear produces the predicted eigenfunction shift. The size of the shift decreases with increasing m, with $\xi_k < \rho_s$ for $\Omega_s = 0.29$ (Fig. 4). The minimum ξ_k gives an upper limit for the radial step size. Although the fundamental scale length in the problem is ρ_s, we must use $\Delta x < \xi_k$ to resolve flow-shear effects properly. We choose $\Delta x = 0.10\rho_s$,

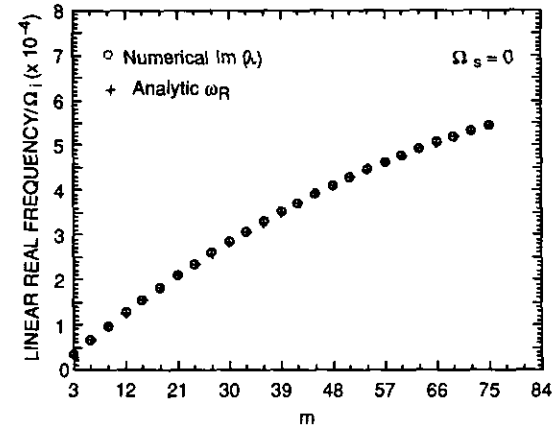

FIG. 3. Analytic real frequency ω_R and numerical eigenvalue Im(λ) for the linear model and small L_s/L_n parameters, as a function of poloidal mode number m. Good agreement is also obtained in the $\Omega_s = 0.29$ case.

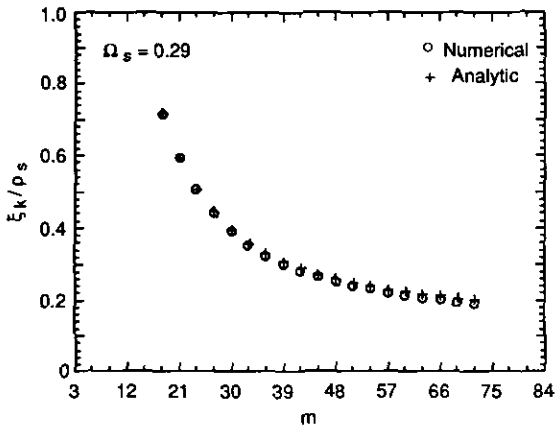

FIG. 4. The flow-shear-induced eigenfunction shift, as a function of poloidal mode number m. The analytic and numerical results agree well, for $\Omega_s = 0.29$ and small L_s/L_n parameters.

in general. Other issues of radial resolution will be taken up in Section V.

One useful property of the implicit linear algorithm is the existence of an optimal time step that greatly accelerates convergence to a particular eigenvalue. This has already been documented for purely growing modes [14], but it also holds for drift waves, which have a real frequency. To see how this property follows from the algorithm, consider the eigenvalue problem equivalent to the linear part of Eq. (13), with eigenvalue $\lambda_{m,n}$:

$$\lambda_{m,n}(L_{m,n}X_{m,n}) = R_{m,n}X_{m,n}. \tag{26}$$

For a given m and n, there is a set of radial eigenmodes characterized by different values of the index l. Assuming that the eigenvectors X_l form a complete and nondegenerate set, iteration using the linear part of Eq. (14) will cause each to evolve with amplification factor $|A_l| \equiv |X_l^{i+1}/X_l^i|$:

$$|A_l|^2 = \left|\frac{1+\lambda_l\frac{\Delta t}{2}}{1-\lambda_l\frac{\Delta t}{2}}\right|^2 = \frac{\left(1+\gamma^l\frac{\Delta t}{2}\right)^2+\left(\omega_R^l\frac{\Delta t}{2}\right)^2}{\left(1-\gamma^l\frac{\Delta t}{2}\right)^2+\left(\omega_R^l\frac{\Delta t}{2}\right)^2}. \tag{27}$$

Here, the eigenvalue λ_l has been related to the growth rate γ^l and real frequency ω_R^l of the original initial-value problem: $\lambda_l = \gamma^l + i\omega_R^l$. The optimal time step $\Delta t^{\text{opt}} = 2/[(\gamma^l)^2 + (\omega_R^l)^2]^{1/2}$ maximizes $|A_l|$. In the purely growing case ($\omega_R^l \equiv 0$), using $\Delta t^{\text{opt}} = 2/\gamma^l$ for any l makes the corresponding $|A_l|$ singular. Growth of the chosen X_l then dominates, and convergence to λ_l occurs within a few steps. In the present case, $\gamma^l < \omega_R^l$ leads to a finite maximum in $|A_l|$ at Δt^{opt} and broadens the resonance. The solution converges to $l = 0$, for which the maximum $|A_l|$ is largest, over a range of time-step sizes (Fig. 5a). Use of $\Delta t^{\text{opt}} \sim 2/\omega_R^0$ still gives the fastest convergence, but the number of steps required is now of the order ω_R^0/γ^0. Thus, time-step size can be used to optimize convergence of the linear algorithm, even with a real frequency.

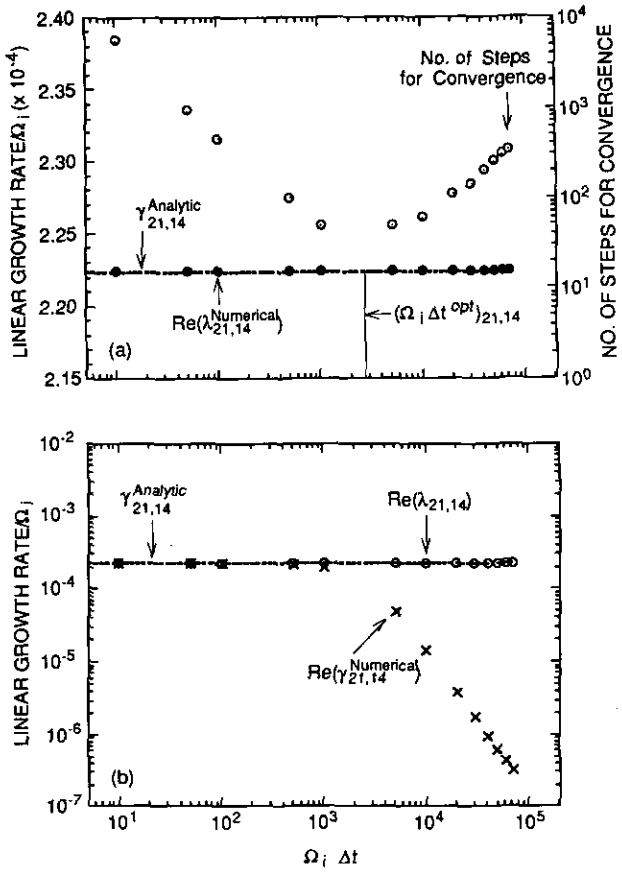

FIG. 5. (a) For m, $n = 21$, 14 and large L_s/L_n parameters, numerical $\text{Re}(\lambda)$ agrees with the analytic γ over a large range of Δt. At an optimal Δt, the number of steps for convergence is a minimum. No converged solution exists for $\Omega_i \Delta t > 7 \times 10^4$. (b) For large Δt, $\text{Re}(\lambda)$ matches the analytic growth rate for m, $n = 21$, 14 and large L_s/L_n parameters. For small Δt, it also agrees with the real part of the numerical growth rate of Eq. (28), thus giving the instantaneous time evolution.

For the linear phase of a nonlinear calculation, convergence is less important than the instantaneous evolution. Iteration of the linear algorithm with $\Delta t \ll \Delta t^{\text{opt}}$ will calculate this correctly. For $\lambda_{m,n}\Delta t \ll 1$, the amount of amplification per iteration is the same as exponentiation at rate $\lambda_{m,n}$. That is, the eigenvalue is close to the numerical growth rate

$$\gamma_{m,n}^{\text{Numerical}} \equiv \frac{1}{\Delta t}\ln\left(\frac{X_{m,n}^{i+1}}{X_{m,n}^i}\right) = \frac{1}{\Delta t}\ln\left[\frac{1+\lambda_{m,n}\frac{\Delta t}{2}}{1-\lambda_{m,n}\frac{\Delta t}{2}}\right]. \tag{28}$$

(See Fig. 5b). Depending on the size of Δt, the same algorithm quickly converges to the linear growth rate or accurately follows time evolution.

V. SPATIAL RESOLUTION AND CONVERGENCE TESTS

Questions of spatial resolution take on greater importance in nonlinear calculations, where small-scale eddies generated by the nonlinear interactions act as an energy sink. The set of Fourier components must include the damped modes at these scales, and Δx must be small enough to resolve the radial structure. Adding an equilibrium flow introduces a new length scale that must be resolved: the eigenfunction shift ξ_k. Information from the linear results of the previous section, such as the size of ξ_k and the boundary between stable and unstable modes in k_y-space, can be used to estimate the appropriate spatial resolution. In this section, we outline the guidelines we have used. Since linear criteria may not always be sufficient in a nonlinear calculation, the resolution requirements have been numerically tested for accuracy and convergence. The results verify that linear guidelines can be relevant when selecting the spatial resolution for a nonlinear calculation.

An upper limit of $\Delta x/\rho_s < 1$ can be imposed on the radial step size. When an equilibrium velocity is present, $\Delta x/\rho_s < (\xi_k)_{\min}$ is needed to resolve the shift in the linear eigenfunction caused by the flow shear. We chose $\Delta x/\rho_s = 0.10$ in the previous section as a result. In a nonlinear calculation, small-scale eddies could reduce this limit even further. However, such a calculation without flow shear shows that $\Delta x/\rho_s = 0.10$ is also sufficient to resolve the radial structure in this case (Fig. 6). Thus, $\Delta x/\rho_s < (\xi_k)_{\min}$ can be used for cases with equilibrium velocity, while $\Delta x/\rho_s < 1$ is a good general limit.

In the presence of an equilibrium velocity, there is also a lower limit on Δx. It is not a numerical condition associated with resolving a physical scale of the system, but concerns excluding nonphysical solutions associated with the particular model we have used. The linear dispersion relation of Eq. (22) predicts that modes with large radial mode number ($l \to \infty$) will be unstable for normalized flow shear above a critical value:

$$\Omega_s^{\text{crit}}(l \to \infty) = 2\left(\frac{\rho_s}{W_k}\right)\left[1 + \left(\frac{k_y^2 D_k}{\omega_{*n}}\right)\right]^{1/2}. \qquad (29)$$

This instability is not a realistic result, but rather, the consequence of a limitation in our model. The assumption of highly collisional ions, used to obtain a single equation, leads to a reduction in linear damping at the largest l. However, Ω_s^{crit} increases as l decreases. Since only those l's that are consistent with the radial resolution are relevant, a minimum Δx can be chosen so that the largest resolvable l is stable for the flow shear of interest. Small k_y gives the most restrictive Ω_s^{crit}, since $W_k \sim k_y^{-1/4}$. Using the smallest k_y, Eq. (22) can be solved to find the stable mode with the largest l for the given value of Ω_s. If this is to be the last resolvable mode, the resolution per peak must be a minimum for the $l+1$ peaks. In this case, the mode width W_k is spanned by one grid point at the left edge, $l+1$ grid points at the peak tops, l grid points between the peaks, and one grid point at the right edge—in all, $2l+3$ grid points. The minimum radial grid size is then $\Delta x = W_k/(2l+3)$. For $m=3$ and large L_s/L_n parameters, the largest resolvable l consistent with our choice of $\Delta x/\rho_s = 0.10$ is about 16. Solutions of Eq. (22) show that modes with $l \leqslant 16$ are stable for all Ω_s used in the numerical calculations. Thus, $\Delta x/\rho_s = 0.10$ satisfies the linear requirements for both the upper and lower limits on Δx.

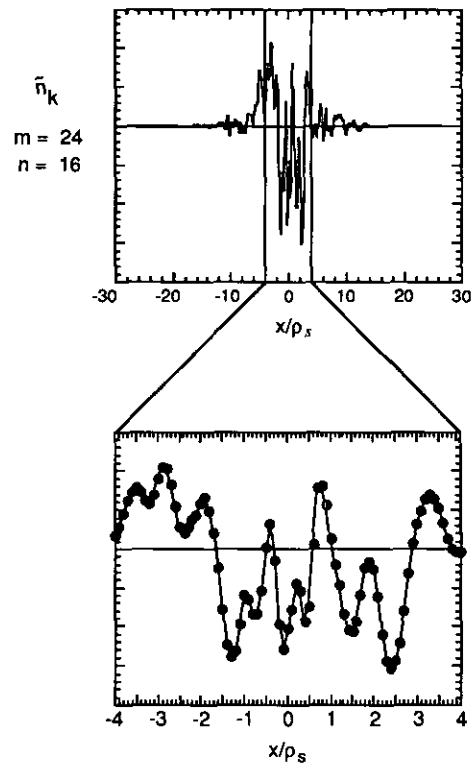

FIG. 6. Radial structure of m, $n=24$, 16 Fourier component during the nonlinear phase of a calculation with multiple rational surfaces, large L_s/L_n parameters, and zero flow shear. The inset shows that this can be resolved with $\Delta x = 0.10\rho_s$.

Tests of convergence with Δx were performed on the numerical solutions. They used large L_s/L_n parameters, slab length $a = 30\rho_s$, time step $dt_0 \equiv \Omega_i \Delta t = 5$, and were centered around the base value of $\Delta x/\rho_s = 0.10$. There were 54 Fourier components along the $m/n = 3/2$ helicity at the single rational surface $r = r_0$. Spatial structure in the nonlinear couplings near the resonant surface causes a reduction in linear damping at small k_y [7] that prevents the fluctuations from saturating. Since the energy (E) grows rapidly, the comparisons use the growth rate $\gamma_E \equiv (2E)^{-1}(dE/dt)$ as a more sensitive measure. Reducing the radial grid spacing to $\Delta x/\rho_s = 0.05$ (without flow shear) or $\Delta x/\rho_s = 0.04$ (with flow shear) leads to a small change in γ_E during the nonlinear evolution (Fig. 7a). This is in sharp

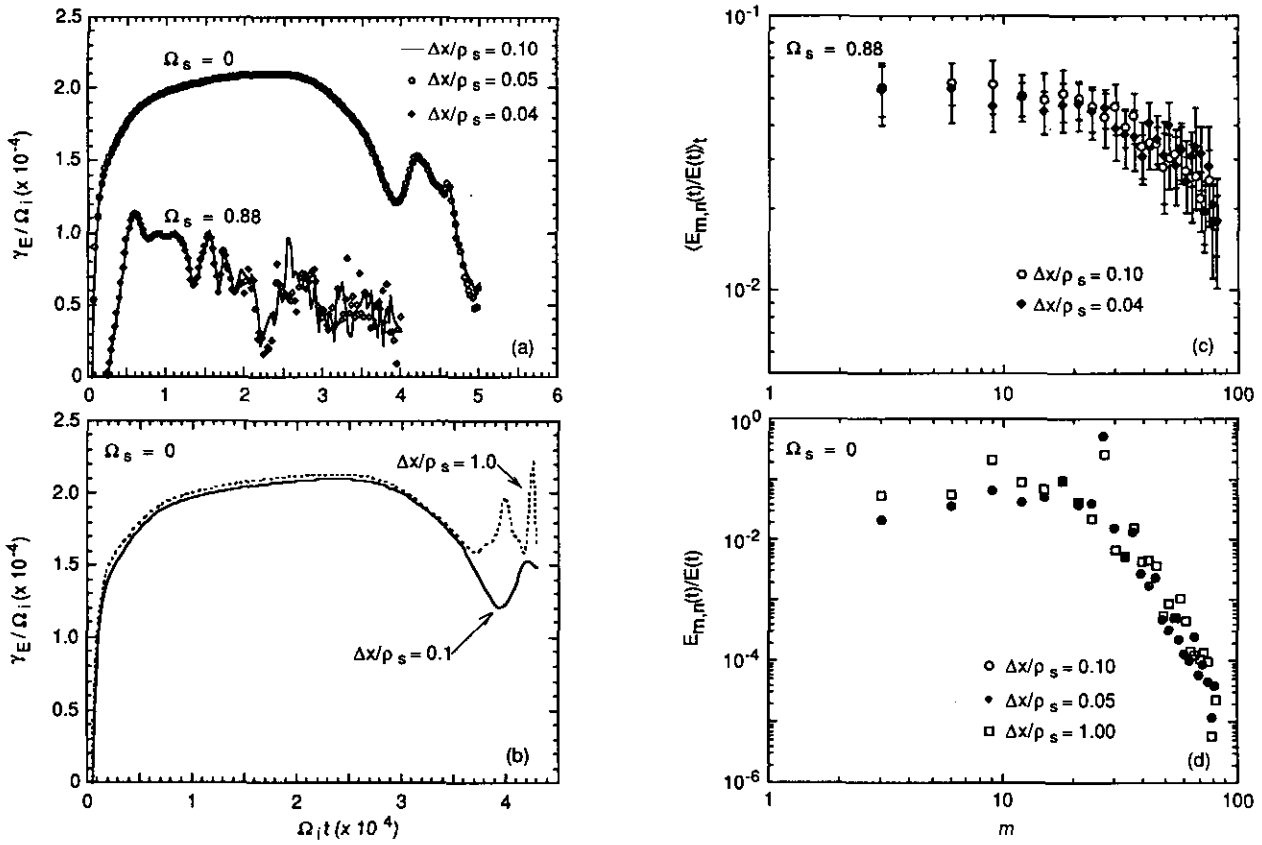

FIG. 7. (a) For calculations with a single rational surface, decreasing Δx by a factor of 2–2.5 does not produce much change in the time evolution of the growth rate γ_E. Since large flow shear ($\Omega_s = 0.88$) produces linear stability, these cases are started at large amplitude to facilitate nonlinear effects. (b) For calculations with a single rational surface, increasing the radial grid spacing to $\Delta x = 1.00\rho_s$ greatly alters the time evolution of γ_E in the nonlinear regime. (c) For calculations with large flow shear ($\Omega_s = 0.88$), decreasing Δx by a factor of 2.5 does not change the energy distribution, $E_{m,n}(t)/E(t)$, given the error bars from time-averaging over $3 \leqslant \Omega_i t \times 10^{-4} \leqslant 4$. (d) For calculations without flow shear, increasing the radial grid spacing to $\Delta x = 1.00\rho_s$ alters the instantaneous energy distribution, $E_{m,n}(t)/E(t)$, at $\Omega_i t \times 10^{-4} = 4.3$ in the nonlinear regime.

contrast to the result of increasing the grid spacing to $\Delta x/\rho_s = 1$. In the zero flow-shear case, γ_E is only slightly altered during the early (single-mode-dominated) phase of the nonlinear evolution. Later, however, it diverges strongly from the value for $\Delta x/\rho_s = 0.10$ (Fig. 7b). Since radial variations in the couplings between the fluctuations prevent saturation, it is also important to verify that the distribution of energy is converged. When energy spectra (normalized to total energy) are compared as Δx is varied, the results are similar to those obtained for γ_E. With flow shear, a reduction in $\Delta x/\rho_s$ produces no change in the spectrum, given the error bars from time-averaging over an interval of stationary γ_E (Fig. 7c). There is no such interval without flow shear, so an instantaneous comparison is made. The spectrum obtained with $\Delta x/\rho_s = 1$ differs markedly from the others, which are virtually identical (Fig. 7d). Thus, $\Delta x/\rho_s < \min(\xi_k, 1)$ appears to be an appropriate guide for obtaining solutions converged with respect to Δx. Within this limit, nonlinear solutions are not very sensitive to variations in radial step size.

The rate of error accumulation in converged cases is small enough to allow nonlinear solutions to remain accurate. For $\Delta x/\rho_s < 1$ and zero flow shear, the spatial discretization error remains below 1% into the nonlinear evolution. In contrast, for $\Delta x/\rho_s = 1$, the spatial discretization error rises to almost 100% in the same interval of time. As Δx varies,

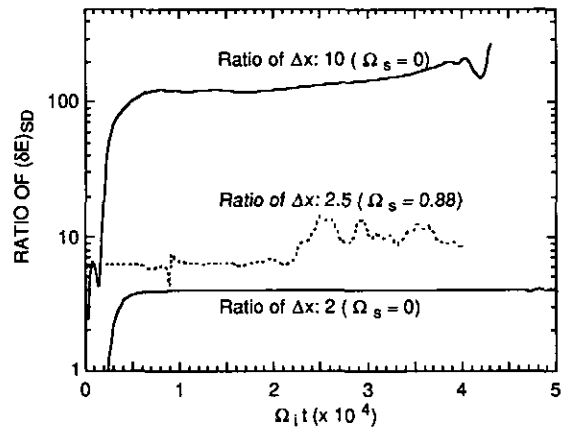

FIG. 8. For cases in which Δx differs by a given factor, the spatial discretization error $(\delta E)_{SD}$ varies as the square of this factor.

the spatial discretization error scales as $(\Delta x)^2$ (Fig. 8). This is consistent with the accuracy of the three-point radial differences used in the algorithm. As a result of this scaling, Δx can be adjusted to reduce the spatial discretization error to a desired level.

Questions of radial resolution must be addressed carefully in the strong flow-shear regime, where Eq. (4) can become singular. When the replacements $\partial/\partial y \to ik_y$ and $\partial/\partial t \to -i\omega$ are made in Eq. (5), the coefficient of $-\rho_s^2 \nabla_\perp^2 \tilde{n}$, the largest radial derivative in Eq. (4), becomes $\omega - k_y V_0(x)$. Writing the Doppler-shifted frequency $\bar{\omega}$ as $\bar{\omega}_R + i\gamma$, this coefficient can be made proportional to $x - z_{\text{sing}}$, where

$$z_{\text{sing}} = W_k \left(\frac{\bar{\omega}_R + i\gamma}{\omega_{*_n}} \right) \left(\frac{1}{\Omega_s} \right). \tag{30}$$

Unstable modes have $\gamma > 0$, and the complex number z_{sing} lies above the real axis. Under these circumstances, the equation is not singular. However, strong flow shear greatly reduces γ for an unstable mode, moving z_{sing} close to the real axis. As the flow shear stabilizes the mode, a singularity at $x = \text{Real}(z_{\text{sing}})$ should appear. It would be of great interest to investigate the performance of the algorithm under these conditions. However, the values of Ω_s that can be used are limited by the critical value of Eq. (29). Above this threshold, there are unrealistic linear instabilities at large l. To avoid such instabilities and ensure meaningful results, we have restricted attention to $\Omega_s < 1$. In these cases, the fluctuations grow, either linearly or nonlinearly. There is no singularity, and the limits on radial resolution discussed above are appropriate. Since the high ion collisionality assumed for this model causes the reduction in linear damping at large l that leads to the instabilities, the large flow-shear regime can be explored only with an improved model.

Next, we estimate the number of Fourier components needed for a resolved calculation. To ensure that the nonlinear evolution is dominated by turbulent energy transfer, there must be sufficient coupling between the energy source and the energy sink. For large L_s/L_n parameters, the growth rates calculated from Eq. (22) show that modes with $3 \leqslant m < 54$ are unstable. For calculations including the single rational surface at $r = r_0$, the maximum m is chosen to be 81. This provides a range of linearly stable modes that can act as an energy sink. Good coupling between the peak of the source ($m = 21$) and the sink is guaranteed by keeping every component along the resonant $m/n = 3/2$ helicity. The total number of Fourier components is then 54, counting both (m, n) and $(-m, -n)$. In a case with multiple rational surfaces, the object is to provide damped modes along each surface and a density of surfaces that permits coupling between modes of different helicities. In practice, a balance is struck between the number of low-order rational surfaces that can be included and the slab size required for them, given a realistic safety factor $q(x)$. The number of components is then determined by selecting the maximum n so that there are damped modes on each surface. We have used a q-profile that includes 129 rational surfaces with resonant helicities between $m/n = 10/7$ and $11/7$. With the maximum n equal to 54, there are a total of 438 components (Fig. 9). (In this case, the rational surface at $r = r_0$ still has the same number of components along the 3/2 resonant helicity.)

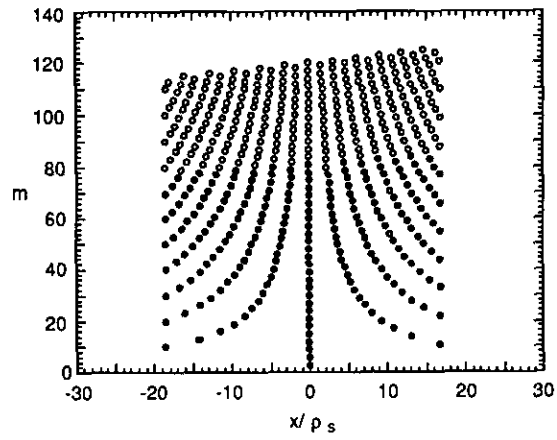

FIG. 9. The radial distribution of Fourier components for numerical calculations with multiple rational surfaces. The closed circles indicate the case with 438 components. The open circles show the additions in the 948-component case.

The number of components in these basic sets was then varied to determine if the damped modes provide a sufficient energy sink at large k_y. In a converged calculation, quantities that depend on sums over components, such as γ_E and the spatial discretization error, should be insensitive to an increase in the number of damped modes. It is also important that the spectrum of squared amplitudes decrease as k_y^{-2}, or faster, in the region of damped modes. Only then can the root mean square (RMS) wavenumber be defined. For a case with a single rational surface, the convergence test consisted of changing the maximum m along the $m/n = 3/2$ helicity. The number of components was increased from 54 to 108 to 216, and the number of linearly damped modes ($m \geqslant 54$) from 20 to 74 to 182. Each case was initialized with a set of components having equal amplitudes and random phases. The initial spatial structure was Gaussian, centered on the rational surface at $r = r_0$, and every component had the same width. The radial step size was $\Delta x/\rho_s = 0.10$, and the other parameters were the same as those used in the Δx convergence tests. The calculations proceeded through a period of nonlinear evolution in which the spatial discretization error was 5% or less.

For the set of 54 components, only the sums over components are converged. In the case of zero flow shear, increasing the number of components to 216 causes only a 30% reduction in a spatial discretization error of less than 1%. With $\Omega_s = 0.88$, the reduction is 5% in a level of about

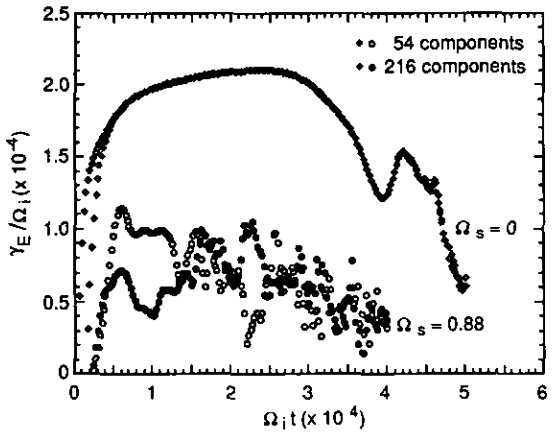

FIG. 10. For calculations with a single rational surface, increasing the number of Fourier components by a factor of 4 does not change the evolution of the growth rate γ_E, on the average.

5%. Furthermore, the addition of modes at large k_y does not produce a significant change in γ_E (Fig. 10). In the case with $\Omega_s = 0.88$, there are some differences in the initial period, during which the mode amplitudes are adjusting themselves in k_y-space, but the later nonlinear growth is very similar, on the average. In contrast, the squared-amplitude spectrum is quite sensitive to these changes. At the end of the calculation with 54 components, the instantaneous spectrum is flat in the region of damped modes. When the number of components is increased to 108, it falls off as $k_y^{-2.7}$. For 216 components, there is some accumulation at the largest k_y, and the fall-off is less steep. Thus, the basic component set cannot produce a converged squared-amplitude spectrum for the damped modes, but the nonlinear couplings between modes with small and large k_y that determine the nonlinear growth rate do not appear to be very sensitive to changes in the number of components.

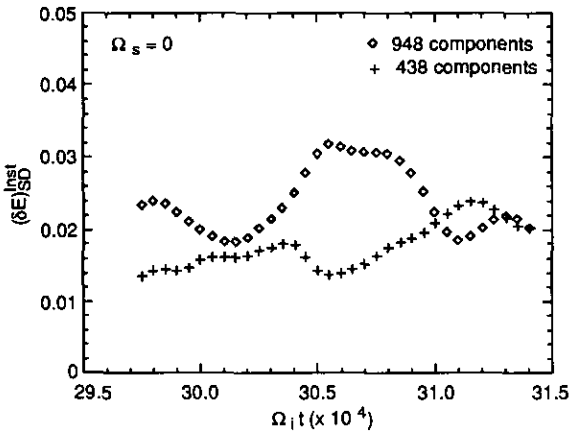

FIG. 11. For calculations with multiple rational surfaces, increasing the number of Fourier components from 438 to 948 increases the instantaneous spatial discretization error $(\delta E)^{Inst}_{SD}$ by an average of 36% in the steady state.

Similar results have been obtained for a calculation with multiple rational surfaces. In this case, coupling between different helicities provides an additional mechanism for energy transfer to damped modes. Saturation can now be achieved, even with fewer damped modes along a particular rational surface. For the basic set of 438 components, the RMS fluctuation level in the steady state is converged, but the time-averaged squared-amplitude spectrum is not. Convergence tests were performed with zero flow shear and small L_s/L_n parameters. The slab length was changed to $a = 60\rho_s$ to accommodate the large number of rational surfaces. A radial step size of $\Delta x/\rho_s = 0.10$ was retained, while $dt_0 = 10$ was used during the nonlinear evolution. The total number of components was changed from 438 to 948 by increasing the maximum n to 80 (Fig. 9). Although this added linearly stable modes to each rational surface, the time-averaged RMS fluctuation level at $r = r_0$ decreased by only 18%. The spatial discretization error in the steady state was also used to test the convergence of sums over components. An instantaneous spatial discretization error was obtained from Eq. (16) for a one-step scheme. At time $t = i\,\Delta t$,

$$(\delta E)^{Inst}_{SD} = \frac{\partial_t E|^{nonlinear}_{i-1}}{|dE/dt| + |SO| + |SK|}. \tag{31}$$

The normalizing terms, defined in Eqs. (19)–(20), use information from time steps i and $i-1$. The first is a difference, and the last two are averages. When the number of components was increased to 948, the average error in the steady state increased by 36% (Fig. 11). This suggests that the energy transfer to damped modes has not been strongly affected. The distribution of damped modes in k_y-space is significantly altered, however (Fig. 12). Although adequate to produce convergence in sums over components, the 438-component set cannot resolve the time-averaged squared-

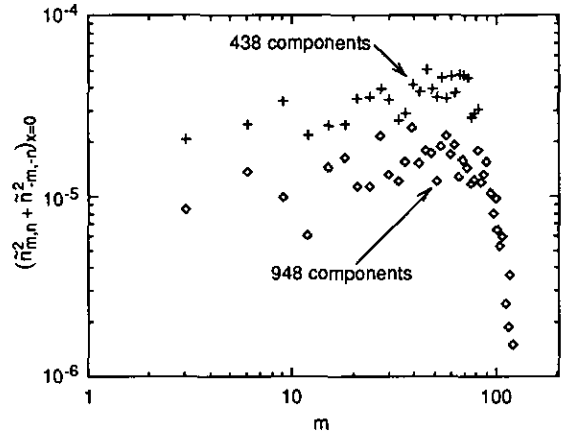

FIG. 12. The decay in the time-averaged squared-amplitude spectrum at large k_y for a calculation with multiple rational surfaces can be resolved with 948 Fourier components, but not with 438 components.

amplitude spectrum. In general, though, grid spacings and component sets chosen according to the guidelines given in this section will be a good starting point for attaining convergence.

VI. TEMPORAL RESOLUTION AND CONVERGENCE TESTS

The final issue to be addressed is the selection of an appropriate time-step size, Δt. As alluded to in Section III, Δt must be small enough to resolve the fastest time scale under consideration. For the linear problem without flow shear, this is given by a real frequency $\omega_R \sim \omega_{*_n} = k_y V_{*_n}$. Although the linear algorithm converges for very large time steps, obtaining a solution becomes more difficult for $\omega_R \Delta t \gg 1$ (Fig. 5a). Thus, we limit ourselves to $\omega_{*_n} \Delta t \sim 1$. This explains the choice of $dt_0 \equiv \Omega_i \Delta t = 10{,}000$ in Section IV. Adding a strong flow introduces a large Doppler shift: $\bar{\omega}_R \sim \omega_{*_n} - k_y V_0(x)$. This imposes a more restrictive requirement on dt_0, which must be small enough to resolve the Doppler-shifted frequency. Since $\bar{\omega}_R$ is a maximum at $x = -(Q/2)$, we choose

$$\bar{\omega}_R \Delta t|_{\max} = (k_y \rho_s|_{\max}) \left[\frac{\rho_s}{L_n} + \frac{\bar{V}_0}{c_s} \left(\frac{a}{2L_V} \right) \right] dt_0 < 1. \quad (32)$$

In nonlinear calculations, the fastest physical phenomena can no longer be described by linear time scales on the order of $\omega_{*_n}^{-1}$. The appropriate scale is associated with the convection of the small-scale eddies. The linear estimate for dt_0 from a case with flow shear, Eq. (32), is too large to use with the nonlinear algorithm, unlike the linear estimate for Δx described in Section V. From experience, $(\omega_{*_n} \Delta t)_{\max} \sim \frac{1}{30}$ has been found to permit stable evolution. This means that $dt_0 \leqslant 10$ for large L_s/L_n parameters.

As the time step is changed from $dt_0 = 5$ to $dt_0 = 0.2$, the numerical solutions do not show much sensitivity. Convergence tests used a single rational surface at $r = r_0$, 54 components along the $m/n = 3/2$ helicity, $\Delta x/\rho_s = 0.10$, large L_s/L_n parameters, and zero flow shear. The one-step algorithm of Eq. (14) was considered first. Reducing the time step from $dt_0 = 5$ to $dt_0 = 1$ changes γ_E by about 16% during the nonlinear evolution. A further reduction to $dt_0 = 0.2$ has little additional effect. With the two-step algorithm of Eq. (15), $dt_0 = 5$ produces an evolution of γ_E identical to that for the $dt_0 = 0.2$ one-step case. Reducing the time step produces no additional difference.

The energy conservation properties of the one-step and two-step algorithms show that each is accurate to the proper order in Δt. The energy conservation error for the one-step algorithm should scale linearly with the time step, since solutions are accurate to order Δt, while the trapezoidal integration of Eq. (21) is accurate to order

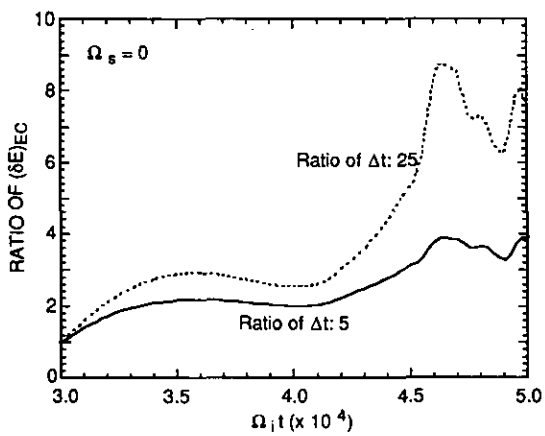

FIG. 13. For cases in which Δt differs by a given factor, the energy conservation error $(\delta E)_{EC}$ has a roughly linear variation with this factor.

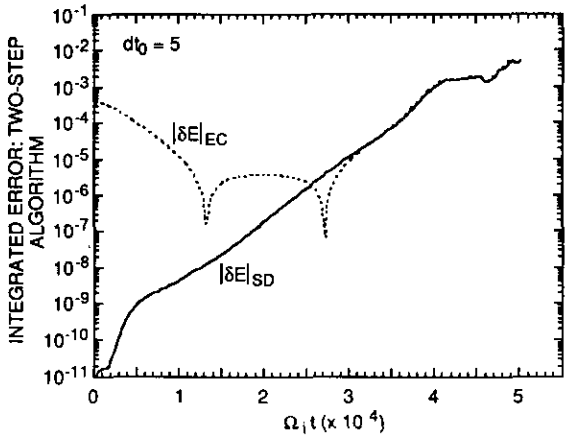

FIG. 14. For the two-step algorithm, the energy conservation error $(\delta E)_{EC}$, which is sensitive to nonzero Δt, asymptotes to the spatial discretization error $(\delta E)_{SD}$, which is not.

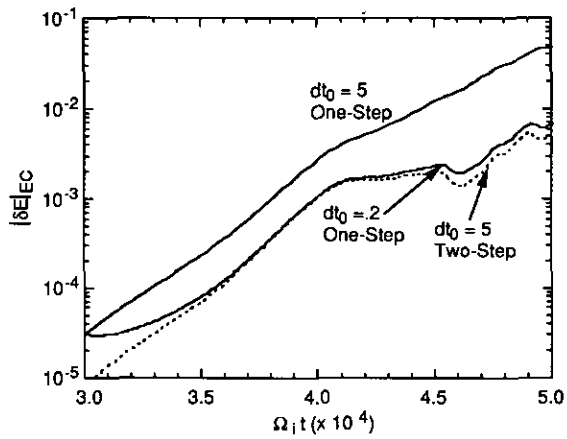

FIG. 15. The energy conservation error $(\delta E)_{EC}$ is reduced by a factor of 10, for the same Δt, on using the two-step scheme rather than the one-step scheme. A similar result could be obtained by reducing Δt a factor of 25 in the one-step scheme.

$(\Delta t)^2$. Changing the time step in the zero-flow case does affect this error, and the scaling is closer to linear than quadratic (Fig. 13). The energy conservation error in the two-step case does not scale with the time step. In this more accurate scheme, the contribution from nonzero Δt becomes smaller than the contribution from finite spatial resolution. This is reflected in the fact that the energy conservation error asymptotes to the spatial discretization error in the nonlinear regime (Fig. 14). However, for a given Δt, two-step results can have less error than one-step solutions. With $dt_0 = 5$, the energy conservation error is about an order of magnitude smaller for the same number of steps in the nonlinear regime (Fig. 15). This error is roughly equivalent to the level in the one-step $dt_0 = 0.2$ case, where the evolution of γ_E is identical. Thus, the two-step algorithm is accurate to an order higher than Δt. The error results support the conclusion that these algorithms can be used to produce accurate nonlinear solutions.

VII. CONCLUSIONS

The focus of this paper has been a single-equation model of long-wavelength drift wave turbulence. The purpose was to present an algorithm that can accurately calculate the time evolution of these waves, which have real frequency $\omega_R \sim \omega_{*n}$, in the presence of a strong poloidal flow with shear. The numerical scheme we have proposed is linearly implicit and nonlinearly explicit. Although the linear part was originally used to calculate purely growing modes, we have demonstrated that it works equally well for modes with a real frequency. Numerical solutions of the model equation agree with the predictions of linear analytic theory for a large range of time steps, up to and including $\omega_R \Delta t \sim 1$. This agreement holds both with and without the sheared flow.

Certain guidelines for choosing the proper resolution for a nonlinear calculation have been proposed. Although the basic length scale is given by the gyroradius ρ_s, a radial step size of $\Delta x/\rho_s < \min(\xi_k, 1)$ is required to resolve both the flow-shear-induced shift in the linear eigenfunction ξ_k and the nonlinear structure. Damped modes are required on each rational surface to act as an energy sink. In estimating the required number of Fourier components, an appreciable fraction of linearly stable modes should be included. Although $\omega_{*n} \Delta t \sim 1$ is adequate for linear drift waves, a smaller time step ($\omega_{*n} \Delta t \sim \frac{1}{30}$) is needed to resolve the nonlinear evolution.

Within these limits, numerical solutions both with and without flow shear are rather insensitive to variations in Δx and Δt. Quantities that depend on Fourier sums do not vary strongly as the number of components is increased, but the spectral falloff at large k_y can be resolved only for the larger numbers of damped modes. The accuracy of the solutions is reflected in the accumulated error, calculated from checks on energy conservation. It remains below 5% into the nonlinear evolution. In addition, this error shows the expected scaling with Δx and Δt, so that it can be reduced to a desired level by adjusting the resolution. Thus, the numerical method described in this paper can be used to calculate the evolution of waves with a real frequency in the presence of strongly sheared flow.

REFERENCES

1. P. H. Diamond, V. Shapiro, V. Shevchenko, Y. B. Kim, M. N. Rosenbluth, B. A. Carreras, K. Sidikman, V. E. Lynch, L. Garcia, P. W. Terry, and R. Z. Sagdeev, in *Proceedings, 14th Int. Conf. on Plasma Physics and Controlled Nuclear Fusion Research, Würzburg, Germany, 1992* (International Atomic Energy Agency, Vienna, 1993), Vol. 2. p. 97.
2. Ch. P. Ritz, T. L. Rhodes, H. Lin, W. L. Rowan, A. J. Wootton, B. A. Carreras, J. N. Leboeuf, D. K. Lee, J. A. Holmes, J. Harris, C. Hidalgo, R. Isler, V. E. Lynch, T. Uckan, P. H. Diamond, A. S. Ware, and D. R. Thayer, in *Proceedings, 13th Int. Conf. on Plasma Physics and Controlled Nuclear Fusion Research, Washington, D. C., 1990* (International Atomic Energy Agency, Vienna, 1991), Vol. 2, p. 589.
3. F. Wagner, G. Becker, K. Behringer, D. Campbell, A. Eberhagen, W. Engelhardt, G. Fussmann, O. Gehre, J. Gernhardt, G. V. Gierke, H. Haas, M. Huang, F. Karger, M. Keilhacker, O. Klüber, M. Kornherr, K. Lackner, G. Lisitano, G. G. Lister, H. M. Mayer, D. Meisel, E. R. Müller, H. Murmann, H. Niedermeyer, W. Poschenrieder, H. Rapp, H. Röhr, F. Schneider, G. Siller, E. Speth, A. Stäbler, K. H. Steuer, G. Venus, O. Vollmer, and Z. Yü, *Phys. Rev. Lett.* **49**, 1408 (1982).
4. R. J. Groebner, K. H. Burrell, and R. P. Seraydian, *Phys. Rev. Lett.* **64**, 3015 (1990).
5. E. J. Doyle, R. J. Groebner, K. H. Burrell, P. Gohil, T. Lehecka, N. C. Luhmann, H. Matsumoto, T. H. Osborne, W. A. Peebles, and R. Philipona, *Phys. Fluids B* **3**, 2300 (1991).
6. H. Biglari, P. H. Diamond, and P. W. Terry, *Phys. Fluids B* **2**, 1 (1990).
7. B. A. Carreras, K. Sidikman, P. H. Diamond, *et al.*, *Phys. Fluids B* **4**, 3115 (1992).
8. P. W. Terry and C. W. Horton, *Phys. Fluids* **26**, 106 (1983).
9. D. Biskamp, in *Turbulence and Anomalous Transport in Magnetized Plasmas*, edited by D. Gresillon and M. A. Dubois (Editions de Physique, Orsay, 1987), p. 239.
10. B. D. Scott, *J. Comput. Phys.* **78**, 114 (1988).
11. R. E. Waltz, *Phys. Fluids B* **2**, 2118 (1990).
12. B. B. Kadomtsev and O. P. Pogutse, *Sov. Phys. JETP* **24**, 1172 (1967).
13. H. R. Hicks, B. A. Carreras, J. A. Holmes, D. K. Lee, and B. V. Waddell, *J. Comput. Phys.* **44**, 46 (1981).
14. L. A. Charlton, J. A. Holmes, H. R. Hicks, V. E. Lynch, and B. A. Carreras, *J. Comput. Phys.* **63**, 107 (1986).
15. L. D. Pearlstein and H. L. Berk, *Phys. Rev. Lett.* **23**, 220 (1969).